# Skull and scalp segmentation in neonatal cerebral MRI using subject-specific probability models

Elham Hokmabadi[a], Hamid Abrishami Moghaddam[a,b,*], Mehrana Mohtasebi[a], Masume Gity[c] , Fabrice Wallois[b,d]

*a Machine Vision and Medical Image Processing (MVMIP) Lab., Faculty of Electrical Engineering, K.N. Toosi University of Technology, Tehran, Iran, b INSERM U1105, Université de Picardie, CURS, Avenue Laennec, 80054, Amiens, France, c Tehran University of Medical Sciences, Tehran, Iran, dINSERM U1105, Unit Exploration Fonctionnelles du Système Nerveux Pédiatrique, South University Hospital, Avenue Laennec, 80054, Amiens, France*

**\*** *Corresponding author*: *Hamid Abrishami Moghaddam, Ph.D., Faculty of Electrical Engineering, K.N. Toosi University of Technology, PO Box 16315-1355, Tehran, Iran (e-mail: moghaddam@kntu.ac.ir).*

## Abstract

This study presents a new approach for the segmentation of cranial bones in magnetic resonance images (MRIs) acquired from neonates in the age range of 39 to 42 weeks, gestational age. This approach uses subject specific probability maps of the skull and scalp, which are created from atlas computed tomography (CT) images taken retrospectively from neonates in the same age range. Our method uses also a subject specific probability map of cerebrospinal fluid (CSF), which is constructed from retrospective atlas MRIs. To construct skull, scalp and CSF probability maps, a subject specific bimodal MR-CT neonatal head template is created (using atlas MR and CT images), and employed. In the next step, the subject specific probability maps are fed to expectation maximization algorithm in conjunction with Markov random field method implemented in FSL software to segment skull and scalp from the input MR image. The results of the proposed method were evaluated through various experiments. First, we computed the similarity between frontal and occipital sutures (reconstructed from segmented cranial bones) and the ground truth (created manually by an expert radiologist). For this purpose, modified versions of Dice similarity index (DSI) were adopted and used. Second, the size of anterior fontanel was compared to its normal size as reported for the neonates in the same age range. Third, the thickness of cranial bones was computed and compared to its normal values as reported for healthy neonates. Finally, a retrospective data including MRI and CT images was used which have been acquired from the same neonate within a short time interval. After aligning the two images, the similarity between cranial bones of the MR and CT image was compared using DSI and modified Hausdorff distance. The results of these experiments demonstrated the success of our segmentation method.

**Keyword:** Magnetic Resonance Image, Computed Tomography image, Subject-specific template, Skull, Neonatal atlas

## 1. Introduction

Skull segmentation in neonatal cerebral magnetic resonance (MR) images is an indispensable and challenging task in neuroscience studies. It has various applications such as providing a realistic head model for source localization from electroencephalography (EEG) or magnetoencephalography (MEG) signals (Kiesler & Ricer, 2003; Li et al., 2015; Nielsen et al., 2018; Okada & Delpy, 2003). Neonatal skull segmentation (stripping) is also required to study brain growth to identify, monitor, and control neuronal diseases (Kiesler & Ricer, 2003; Nielsen et al., 2018). However, the MR imaging (MRI) modality is primarily useful for soft tissue differentiation since cranial bones are weakly represented due to their low

water content. This inconvenience is more pronounced in neonatal cerebral MRI versus adults due to fine and incomplete skull structure. Additional specific challenges in neonatal skull segmentation in MRIs are the presence of higher motion artifact and the small head size of the newborn. Scanning at higher resolution leads to higher noise levels (Prastawa et al., 2005) and more chemical shift artifact (Weinreb et al., 1985). Consequently, neonatal skull in MR images appears with variable thickness and heterogeneous intensity in contrast to the adult skull which is represented as a thick and specific intensity structure. Accordingly, the skull segmentation methods developed for MRIs acquired from adults generally fail to perform accurately in neonates. On the other hand, computed tomography (CT) of the neonatal head is ideal for skull segmentation because it provides better contrast between the cranial bones and remaining tissues (Li et al., 2015). However, it fails to resolve cerebral soft tissues which are mandatory for neuroscience studies. Furthermore, due to its harmful ionizing radiation, CT scans can be acquired from neonates only when it is inevitable for clinical purposes (Mohtasebi et al., 2021).

The lack of reliable ground truth for validating the results is another main obstacle against the development of accurate skull segmentation methods in neonatal cerebral MR images. Manual or semi-automatic skull segmentation performed by expert radiologists on image slices is mostly used to provide ground truth in adults' or children's cerebral MRIs. However, this technique is impracticable in cerebral MR images acquired from neonates due to the above-mentioned challenges which make the concerned structure quasi-imperceptible on two-dimensional slices. Therefore, new ideas inspired by anatomical knowledge and imaging technology are required to provide faithful landmarks and ground truth from three-dimensional MR data and smooth the path for developing accurate neonatal skull segmentation methods. The MR image intensity in a region of interest depends on the pulse sequence used and tissue type. Some tissues with high water content as in edema, tumor, infarction, inflammation, infection, hemorrhage (hyperacute or chronic) appear dark on T1-weighted images (Keith A. Johnson). In contrast, some tissues such as fat, subacute hemorrhage, melanin, protein-rich fluid, slowly flowing blood, paramagnetic substances (gadolinium, manganese, copper), and laminar necrosis of cerebral infarction appear bright on T1-weighted images ( Keith A. Johnson). The process of calcification of tissues in MR images generally has either a null effect or is seen as a reduction in signal intensity and darkening of the tissue ( Keith A. Johnson) Reciprocally, Henkelman et al. (Henkelman et al., 1991) showed that in some cases it is displayed brightly and at high intensities. In neonatal T1-weighted MRIs, some sutures are visible as bright spots in specific slices due to ossification. The bright spots can be distinguished via intensity filtering and examining the adjacent slices along with the three-dimensional views and used as anatomical landmarks for validation of the skull segmentation results. An alternative validation method is to compare the results of skull extraction from MR and CT images which have been acquired within a short time interval from the same subjects. Obviously, such a bimodal data from neonates with anatomically normal head is rarely available in medical archives because it can be acquired only for clinical purposes. In this regard, Nielsen et al. (Nielsen et al., 2018) assessed the accuracy of skull extraction results from MR images by comparing CT-based skull segmentations on a group of adult subjects.

Despite the necessity of accurate scalp and skull segmentation in neonatal MR images, there are few published methods in this field mainly because of the above-mentioned challenges. In this context, Burguet et al. (Burguet et al., 2004) created realistic models of children's heads from 3D-MRI segmentation using a watershed algorithm. Despotovic et al. (Despotovic et al., 2009) extracted scalp, fat, skull, cerebrospinal fluid (CSF), and brain tissues from a 39-week-old newborn T1 image using a hybrid algorithm that included active contours, fuzzy C-means clustering, and mathematical morphology. Daliri et al. (Daliri et al., 2010)

extracted skull from infants' MRI using a Hopfield neural network and a fuzzy classifier. Yamaguchi et al. (Yamaguchi et al., 2010) proposed a fuzzy-logic-based method for skull stripping in children's MR images. Mahapatra et al. (Mahapatra, 2012) used prior shape information within a graph cut framework for skull stripping of neonatal cerebral MRI. To improve the skull removal from pediatric MR images, Shi et al. (Shi et al., 2012) developed a brain-extraction meta-algorithm and integrated it into the analysis and neonatal brain extraction toolbox (iBEAT). Noorizadeh et al. (Noorizadeh et al., 2019) presented a multi-atlas patch-based label fusion method for automatic brain extraction from T2-weighted neonatal MR images. Most of the above methods suffer from unrealistic and low accuracy rates of neonatal skull segmentation results. This low performance is expected and comprehensible for the methods which use low-level image processing tools (Burguet et al., 2004; Despotovic et al., 2009; Yamaguchi et al., 2010), because they rely on image intensities for discerning between tissues whereas the skull is quasi-imperceptible in neonatal MR images. Artificial intelligence-based and atlas-based methods (Daliri et al., 2010; Mahapatra, 2012; Noorizadeh et al., 2019; Shi et al., 2012) on the other hand yielded unsatisfactory results, mainly due to imperfection of their skull geometry knowledge-base.

In the current study, we develop a new method to extract the skull and scalp from neonatal T1-weighted MRI by taking advantage of a realistic and accurate skull model created using a retrospective CT dataset. Cherel et al. (Cherel et al., 2015) proposed subject-specific atlases of manually segmented images in their database and used individual images as reference. Inspired by (Cherel et al., 2015), subject specific probability tissue maps are generated based on the MRI and CT atlas population in the age range of 39 to 42 weeks gestational age (GA). Then for skull extraction, the EM algorithm in conjunction with Markov random field (MRF) implemented in FSL software was used (Smith et al., 2004). The computed subject-specific atlases were well adapted to the subjects to be segmented. An overview of the proposed methodology is shown in Figure 1.

The probability maps of skull and scalp from CT images were constructed and used as a priori information alongside CSF probability map to extract skull and fontanels from MR images. Adaptation of this model and the input MR image to be segmented, is the advantage of this method. In other words, having this bias of the template relative to the input image helps to improve segmentation results.

## 2. Materials and methods

### 2.1 Subjects and Data Acquisition

In our retrospective study, two databases of MR and CT images have been used. All the images were examined by our expert radiologist and no serious cerebral anatomical abnormality was detected. The MRI database was employed to construct geometric and probability models of newborn heads. The images in this database have also been used as test images as will be described hereafter. The CT dataset was also used to build geometric model of the neonatal head and probability models of the skull and scalp. In the following, these two datasets are introduced, respectively.

**MRI database:** The MRI data employed in this study were exactly the same as used in (Kazemi et al., 2007). The subjects in the MRI database were 14 newborns of GA between 39 and 42 weeks at the date of MR examination and were partitioned into two subsets. The first subset consisted of 7 subjects, including 4 girls and 3 boys which were used to create a geometric model. These images have also been used as test

images within a leave-one-out cross validation strategy. The second subset consisted of 7 MRIs including 3 girls and 4 boys that were used only for evaluating skull segmentation results.

Twelve newborns were imaged by a General Electric 1.5T machine using the following sequence parameters: TR=10.1 ms, TE=2.208 ms, TI=500 ms. Each volumic image had $512 \times 512$ pixels per slice with a 220 mm field of view with a voxel size of $0.47 \times 0.47 \times 0.47$ mm$^3$. The two remaining images were obtained by a Siemens 3 T MR scanner with the following sequence: TR=1820 ms, TE=4.38 ms, and TI=1100 ms. Each volumic image had $256 \times 256$ pixels per slice with a voxel size of $1 \times 1 \times 1$ mm$^3$. Then, to reduce the computation time, all images were re-sliced to $0.94 \times 0.94 \times 0.94$ mm$^3$ using the trilinear interpolation method in SPM software.

An ideal data for the evaluation of our skull segmentation method is a bimodal MR-CT image acquired simultaneously from a normal subject. Such ideal data being rarely available, we used a CT image of a subject with the age of 40 weeks GA and an MR image of the same subject at 42 weeks GA. The CT and MR image resolutions were $0.32 \times 0.32 \times 0.63$ mm$^3$ and $0.5 \times 0.5 \times 0.5$ mm$^3$, respectively.

**CT database**: The images used in this study were exactly the same images as used to build the CT atlas in (Ghadimi et al., 2015; Ghadimi et al., 2017; Mohtasebi et al., 2021). The dataset contains 16 CT images including 12 boys and 4 girls of infants aged from 39 to 42 weeks at the date of examination (GA). All the images were acquired using a LightSpeed 16, GE Medical Systems. The imaging matrix was $512 \times 512$ pixels. The voxel size was between $[0.26\text{-}0.49] \times [0.26\text{-}0.49] \times [0.6\text{-}1.25]$ mm$^3$ with a median of $0.32 \times 0.32 \times 0.63$ mm$^3$. Similar to MRIs, all non-axial images were reoriented to the axial plane and re-sliced to $0.94 \times 0.94 \times 0.94$ mm$^3$ isotropic voxels. There was no subject in common between MR and CT databases which have been used for geometric and probability model creation.

## 2.2 Atlas data preparation

According to Figure 1, the neonatal skull segmentation algorithm receives three inputs including neonatal MR input data, MR atlas data and CT atlas data.

### 2.2.1 MR atlas data preparation

Neonatal MR atlas data provide a part of anatomical a priori information for the skull segmentation algorithm. Before being fed to the algorithm, the MR atlas images underwent several semi-automatic preprocessing stages. The neck and extra parts of the head were removed manually using 3D Slicer software (Fedorov et al., 2012). Then, noise elimination, rotation, bias correction, and histogram matching were performed. The bias correction was done by the N4 algorithm (Tustison et al., 2010). Finally, the images were smoothed using a 2 mm Full Width at Half Maximum (FWHM) Gaussian kernel. The intracranial and CSF have already been segmented automatically followed by manual corrections (Kazemi et al., 2008) and were examined by our expert radiologist and available in the database.
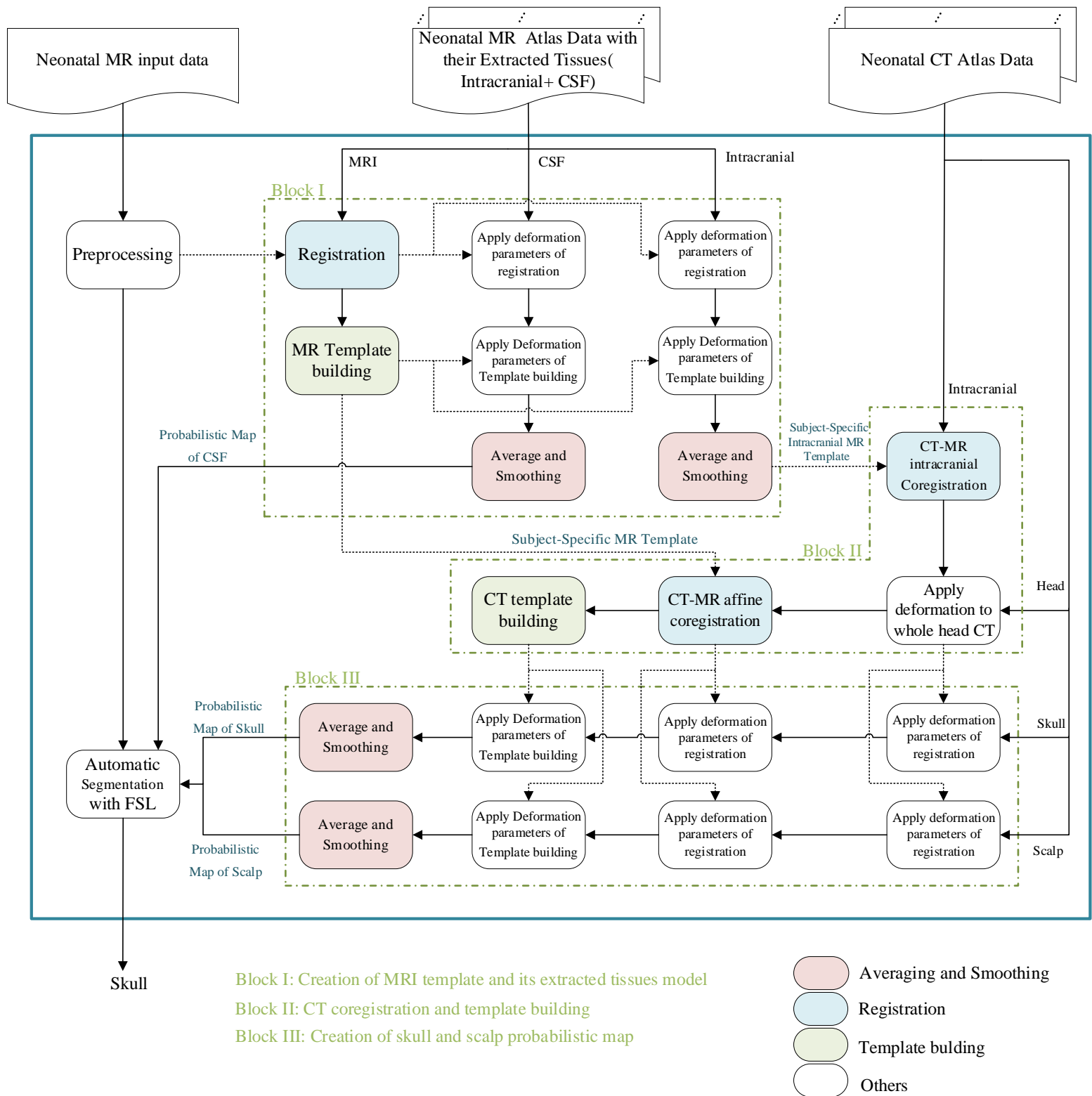
**Fig. 1.** Flowchart of the proposed pipeline to extract skull from neonatal cerebral MR image

### 2.2.2 CT Atlas data preparation

CT atlas data complement the anatomical a priori information for the neonatal skull segmentation method. CT atlas images undertook a number of preprocessing steps before being fed to the skull segmentation algorithm. First, the neck and extra parts of the head were removed using MRIcron software. Then all CT images were manually translated and rotated using 3DSlicer software to get relative alignment with the subject-specific MR template. It is necessary to consider extreme attention to accurate alignment of these images, to achieve high-quality models of the skull. After manual alignment, some background pixels corresponding to air receive zero intensity (instead of -1000) which represents certain tissues inside the brain. Also, some unwanted structures such as pacifiers, masks on the infant's mouth, tubes, neck, and noise around the image, which are visible in some CT images must be removed manually. To solve the aforementioned problems, it is necessary to extract the head mask of the input raw image. For this purpose, we isolated the head from the background on the input raw image using the histogram thresholding (Otsu, 1979) method and morphology operators such as opening, closing, filling, and identifying connected components. Then, by multiplying the head mask by the CT image, everything inside the head retained its intensity and everything in the background of the CT image received zero intensity. In CT images, CSF and the background have the same intensity equal to zero. To distinguish between CSF and background in CT images, we assigned an intensity of -1000 to each voxel in the background. Then, the intensity of the CT images was transformed from the Hounsfield unit to the Cormack unit using a reversible mapping proposed by Rorden et al. (Rorden et al., 2012). This intensity transformation enlarges the dynamic range of the soft tissues and gets the intensity of CT images closer to the intensity of MR ones and increases the accuracy of registration.

After pre-processing, it is necessary to extract the intracranial, scalp and skull tissues from CT atlas population. To extract the intracranial tissue from CT atlas images, the method proposed by Ghadimi et al. (Ghadimi et al., 2017) was used. First, to find the inner surface of the skull, the coupled level sets algorithm (Ghadimi et al., 2015) was used. The resulted surface (inner surface of the cranial bone and sutures) was assumed to be the outer surface of the intracranial tissue. After manual correction by a specialist, a mask was created by the filling operator and employed to extract the intracranial from the CT image. Figure 2 shows the process of extracting intracranial tissue from a CT image. The skull extraction was performed by the histogram thresholding using Otsu's method (Otsu, 1979).

To extract the scalp from the CT images, the fontanels and sutures which are the intersection of inner and outer skull contours were reconstructed using the coupled level sets algorithm (Ghadimi et al., 2015). After a manual correction in some cases, we created a continuous surface from the skull using logical OR operation between skull and reconstructed fontanels. Then, the outer contour of this surface was found by the coupled level sets algorithm (Ghadimi et al., 2015). A mask of this contour was created by the filling operator. Finally, this mask was employed to remove all areas inside the skull along with the cranial tissue itself. Figure 3 shows the process of extracting the scalp tissue from a CT image.

## 2.3 Skull segmentation Algorithm

### 2.3.1 Preprocessing of the input MR image

The skull segmentation algorithm receives a neonatal cerebral MR image as input. As shown in Figure 1, this image was preprocessed in order to be prepared for further processing. The preprocessing stage was explained in Section 2.2.1.
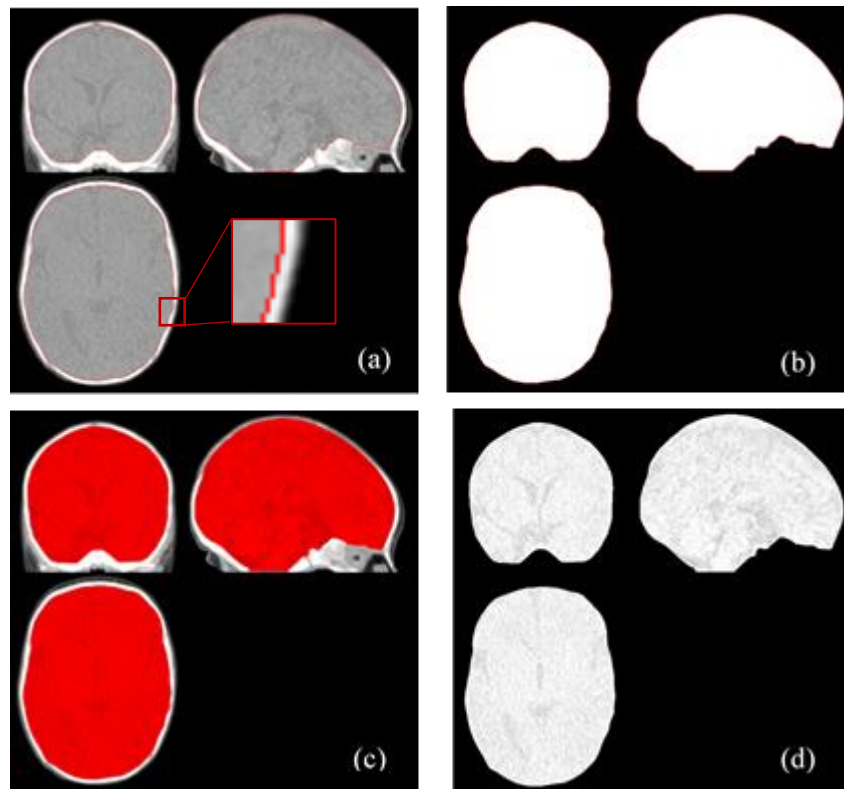
**Fig. 2.** Extraction of CT intracranial tissue using the method proposed in (Ghadimi et al., 2015) a) The extracted inner surfaces of cranial bones b) Corresponding mask of the resulting inner contour c) The extracted mask overlaid on the CT image d) The final extracted intracranial
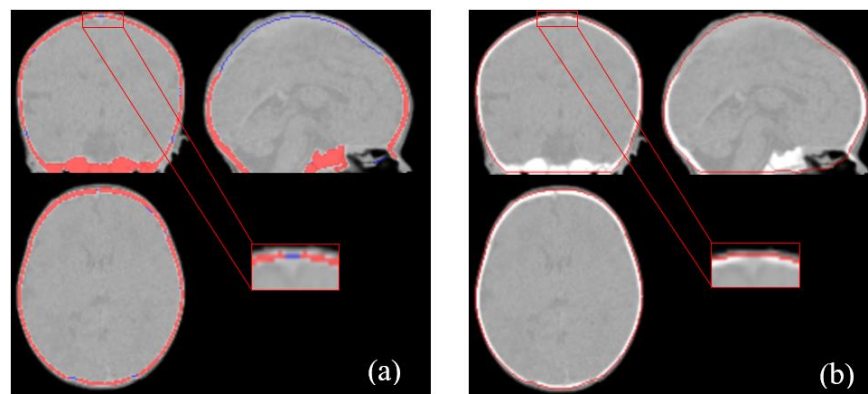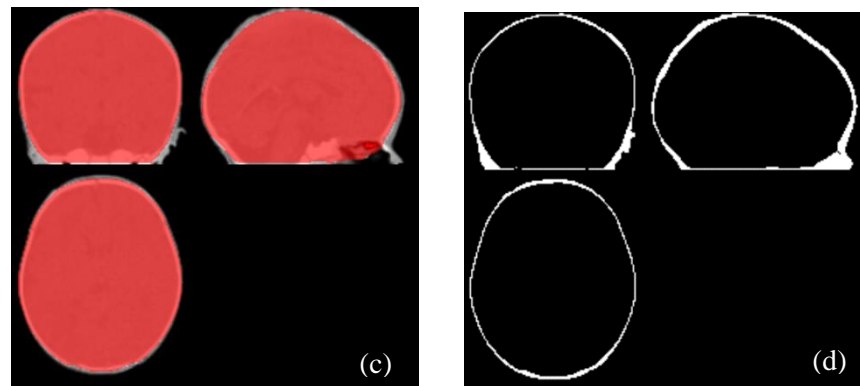
**Fig. 3.** Extraction of CT scalp tissue. a) The reconstructed fontanels (blue) with cranial bones (red) overlaid on the CT image b) Outer contour of the obtained closed surface of the skull c) The corresponding mask overlaid on the CT image d) The final extracted scalp

### 2.3.2 Creation of subject-specific MR atlases

As shown by Block I in Figure 1, the MR atlas images in the database were mapped to a reference space to construct a subject-specific geometric model of the head as suggested by (Cherel et al., 2015). Accordingly, the MRI of the subject to be segmented was selected as reference and each subject in the MR atlas population was registered to it using first a rigid, then a non-rigid transformation. In the first step, a 12-parameter affine (including translation, rotation, scaling, and shearing) transformation was applied to align linearly the MR atlas population with the reference space. In the second step, a nonlinear symmetric normalization (SyN) transformation (Avants et al., 2008) was deployed to match the linearly mapped MR images to the reference. All the deformations have been applied using ANTs software which has been implemented within the framework of the ITK open-source tool (Avants et al., 2014). Also, the transformation parameters obtained during registration were applied to the extracted tissues of each MR image in the database including intracranial and CSF. The objective was to align these tissues with the desired reference as well. A groupwise registration approach (Avants et al., 2014) was subsequently applied to create a MR template. This method is available in ANTs software via the script "antsMultivariateTemplateConstruction.sh". It was run for two iterations using cross-correlation (Lemieux et al., 1998) as similarity index and SyN energy term to construct a subject-specific MR template.

Then, the mapped intracranial and CSF tissues were transformed into the MR template's space by applying the deformation parameters obtained during template building. It is noteworthy that the CSF tissue has been extracted in binary format. Finally, the obtained tissues were averaged and smoothed by a Gaussian filter with FWHM=2mm. In this way, an intracranial geometric model and a CSF probability model were constructed. A probability atlas of a tissue is a 3D image with the same size as the MR (or CT) template. In the probability atlas, the value of each voxel $\vec{x}$ represents the probability of presence of the $i$th tissue $P_i(\vec{x})$ in the same voxel of the corresponding template. Figure 4(c) shows the intracranial MR template which was created in this section for the subject to be segmented. Likewise, Figure 4(d) shows the CSF probability map which was created for the same subject.
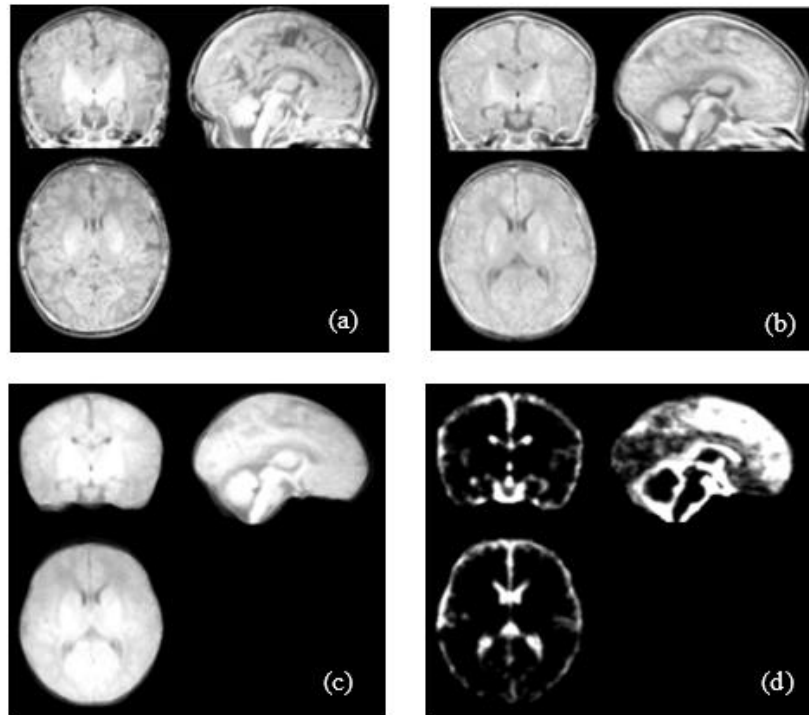
**Fig. 4.** Subject-specific MR templates for subject N3 a) MRI of subject N3 b) Whole head MR template c) Intracranial MR template d) CSF probability model
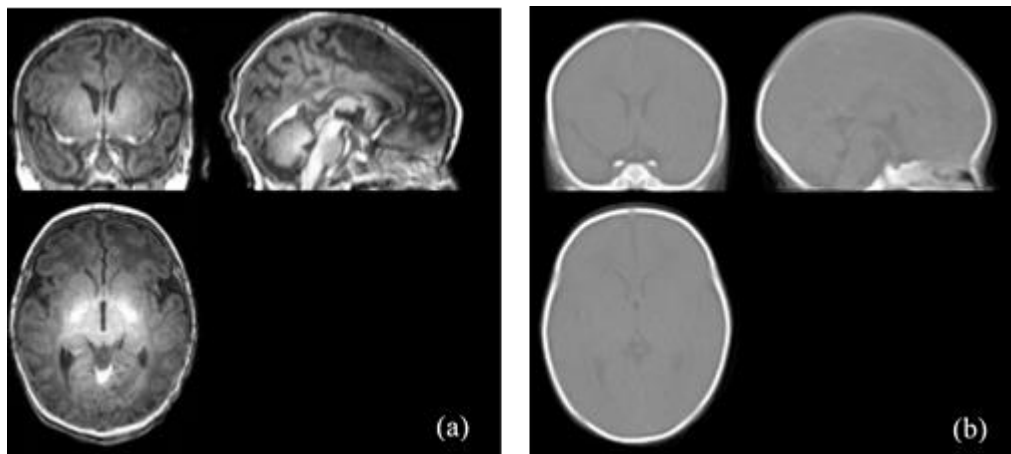
### 2.3.3 Creation of subject-specific CT atlases

As shown by Block II in Figure 1, to construct a subject-specific CT template corresponding to the input MRI, the method proposed by Ghadimi et al. (Ghadimi et al., 2017) was used. The only difference between our method and theirs was the choice of reference space for mapping the images. In this research, the reference space was the geometrical templates made in Section 2.3.2. Therefore, for each input MRI to be segmented, it was necessary to map all atlas CT images to the new subject-specific space represented by the full head and intracranial MR templates which were constructed in Section 2.3.2.

**CT-MR Co-registration:** The mapping of atlas CT images to the subject-specific full head and intracranial MR templates consisted of three main steps:

1. First, the atlas CT intracranial images were linearly and nonlinearly transformed to the subject-specific intracranial MR template, using 12-parameter affine and SyN transformation (Avants et al., 2008), respectively. Mutual information (MI) was used to match the CT intracranial images to subject-specific MR intracranial template.
2. Second, the linear and nonlinear transformation matrices resulted from mapping of each atlas CT intracranial image were applied to its original whole head image.
3. Third, the resulted whole head CT images were registered to the subject-specific MR template using an affine transformation and employing the MI index.

**Subject-specific CT template building**:  At this step, the CT atlas images which have been successfully mapped to the subject-specific MR template, were employed to construct the subject-specific CT template. The procedure was similar to building a MR template as described in Section 2.3.1. Figure 5 shows a CT template which has been constructed for one of the MR tests subjects.



**Fig. 5.** a) MRI of subject N3. b) The specific CT template for this subject

### 2.3.4 Creation of subject-specific probability maps of neonatal skull and scalp

To create the probability maps of the skull and scalp tissues, the atlas CT skull and scalp images which have been prepared in Section 2.2.2 (CT atlas data preparation) were used (see Block III in Figure 1). First, the transformation parameters obtained during whole head CT-MR coregistration were applied to the CT atlas skull and scalp images. The objective was to align the images of these tissues with the subject-specific MR template. Second, the mapped skull and scalp tissues were transformed to the CT template's space by applying the deformation parameters acquired during CT template building. Finally, the mapped images of the tissues were averaged and smoothed with a Gaussian filter via FWHM=2mm. Figure 6 and 7 show the subject-specific probability model of skull and scalp which have been constructed for one of the MR tests subjects.

### 2.3.5 Skull segmentation from the input MR image

Having created the subject-specific probability maps of the skull, scalp (Section 2.3.4), and CSF (Section 2.3.2), the skull can be segmented from the preprocessed input MR image using FAST toolbox of conventional FSL software (Smith et al., 2004). In the FAST toolbox, the EM algorithm in conjunction with Markov random field have been implemented. Also, the subject-specific neonatal probability maps constructed using MR and CT atlas images were used for segmentation (instead of using the FSL default models). Since the preprocessed input image and the subject-specific probability maps were in the same space, the identity matrix was used for mapping the input image to the probability models. Depending on the input image, the probabilities of less than 0.3 or 0.4 in the probability maps were considered as zero. The output of this step was the binary masks of the skull, scalp, and intracranial, which is shown in Figure

8(a). The binary skull mask was extracted using histogram thresholding (Figure 8 (b)). In some cases, post-processing of the extracted skull such as noise elimination, correction of some depressions in the surface of the skull, and removal of some pixels which were mistaken as skull tissue was required.
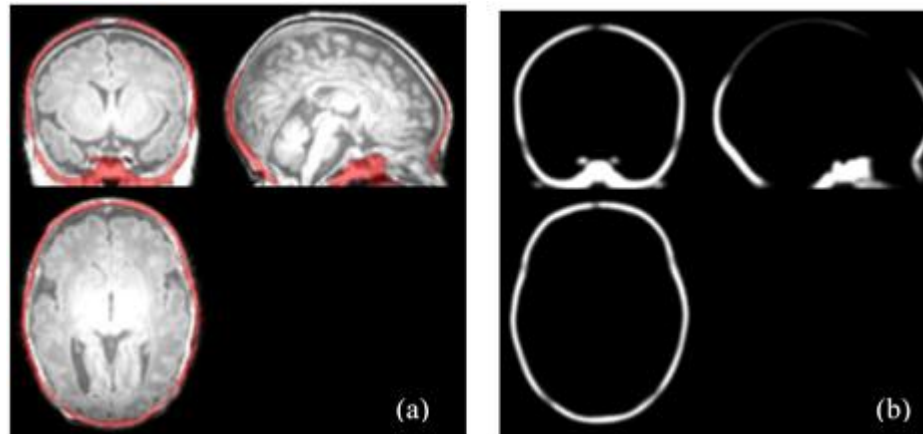


**Fig. 6.** a) The subject-specific probability model of skull overlaid on the MRI of subject N2. b) The specific probability model of neonatal skull for this subject
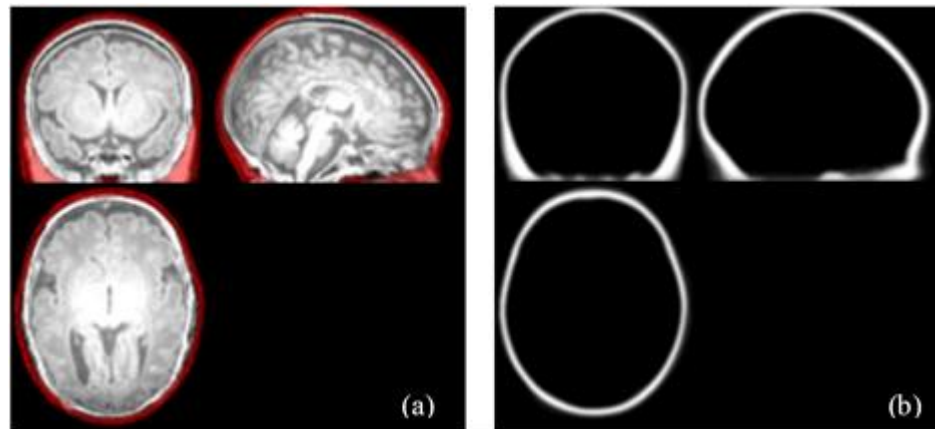


**Fig. 7.** a) The subject-specific probability scalp model overlaid on the MRI of subject T4. b) The specific probability model of neonatal scalp for this subject
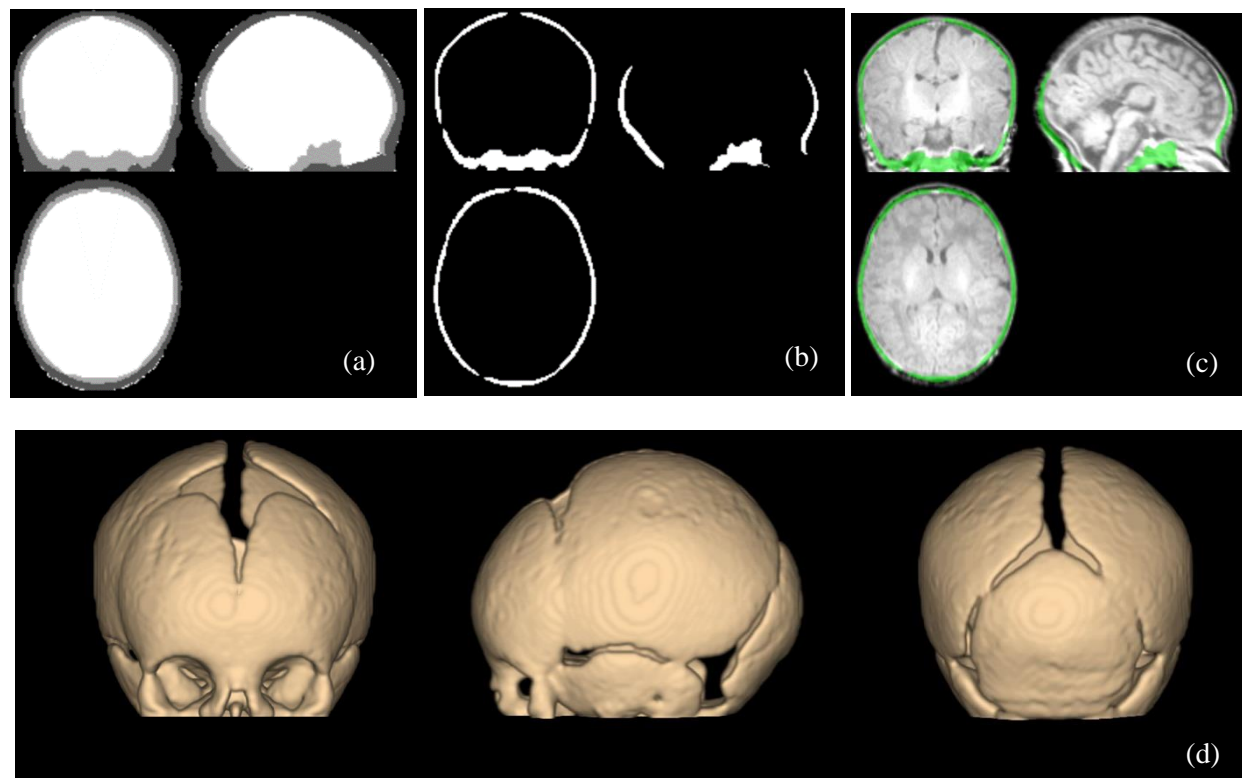
**Fig. 8.** a) Results of the FSL software. b) The final extracted skull for subject T2 c) Extracted skull overlaid on MRI d) Three-dimensional rendering of the segmented skull

## 2.4 Evaluation methods

A ground truth is mandatory to validate the results of skull segmentation from neonatal MR images. It is often created using the manual segmentation of images by an expert. However, manual segmentation of cranial bones in neonatal MR images is a too complex and time-consuming task due to the lack of reliable intensity information of skull, sutures, and fontanels in 2D slices. Therefore, to evaluate the proposed method, the anatomical landmarks on the 3D surface of the head in the MR image are used (Li et al., 2015). Furthermore, CT images can be used as the required ground truth in subjects whose MR and CT images are available within less than two weeks apart; since the cranial tissues can be easily extracted in CT images. In this section, four scenarios are presented to evaluate the results of the neonatal skull segmentation method.

### 2.4.1 Evaluation of the results using 3D anatomical landmarks

Figure 9 shows how metopic and coronal sutures appear in the axial view of a T1-weighted MR image. The zoomed-out parts in Figure 9 help to better illustrate these anatomical landmarks. In this paper, to extract the bright spots that will be labeled as sutures, MRIcroGL software was used. Since different tissue types have different image intensities, thresholding the intensity and changing "transparency" in 3D volume rendering, can reveal the desired tissues while making transparent other tissue types. In each slice, a square was considered around the desired anatomical landmark. In this square, pixels with high intensity were

labeled as sutures. Figure 10 (a) shows that the sutures are visible as bright tracks in the 3D view of the head. In Figure 10 (b), the voxels of the image were labeled as sutures with the aforementioned method. It is noteworthy that all extracted anatomical landmarks were approved by a specialist.

After extracting the visible sutures in the MR images, the accuracy of the results can be validated qualitatively and quantitatively by examining the correspondence between the position of these landmarks and the extracted cranial bones. Figure 11 shows the position of manually extracted sutures on MR axial slices of a test subject.

To quantitatively evaluate the results, we first reconstructed the fontanels from the extracted cranial bones using the coupled level set algorithm (Ghadimi et al., 2015). Then, we calculated the similarity in shape between the ground truth landmarks and the reconstructed fontanels. Dice similarity index (DSI) is almost used for this purpose. However, landmarks and fontanels are narrow and thin structures distributed three-dimensionally as a small part of the neonatal skull. This is why DSI does not exactly match our requirements for this specific evaluation problem. Therefore, we defined and used a modified similarity index (MSI) as the number of corresponding landmark and fontanel voxels divided by the number of landmark voxels. Strictly speaking, two correspondent voxels must have the same coordinates in both landmark and fontanel images. However, by generalizing the correspondence to the first and second nearest neighbor, two variants of MSI called MSI_1 and MSI_2 were obtained and used in this study. Algorithm 1 was used to compute MSI, MSI_1 and MSI_2. Figure 14, shows qualitatively the match between the position of anatomical landmarks (anterior and posterior sutures) and fontanels which have been reconstructed by the coupled level set algorithm (Ghadimi et al., 2015). Both of the structures were overlaid on cranial bones which have been segmented by the proposed algorithm.
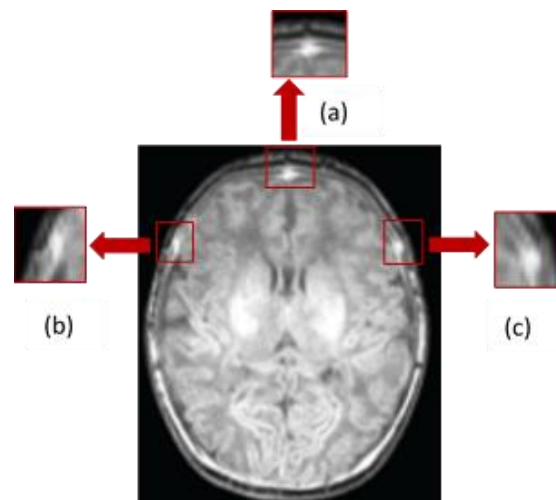


**Fig. 9.** Axial view of the MR image of the subject N1. The bright spots enclosed by red rectangles show how sutures appear in a $T_1$-weighted MRI. a) Metopic suture b, c) coronal sutures.
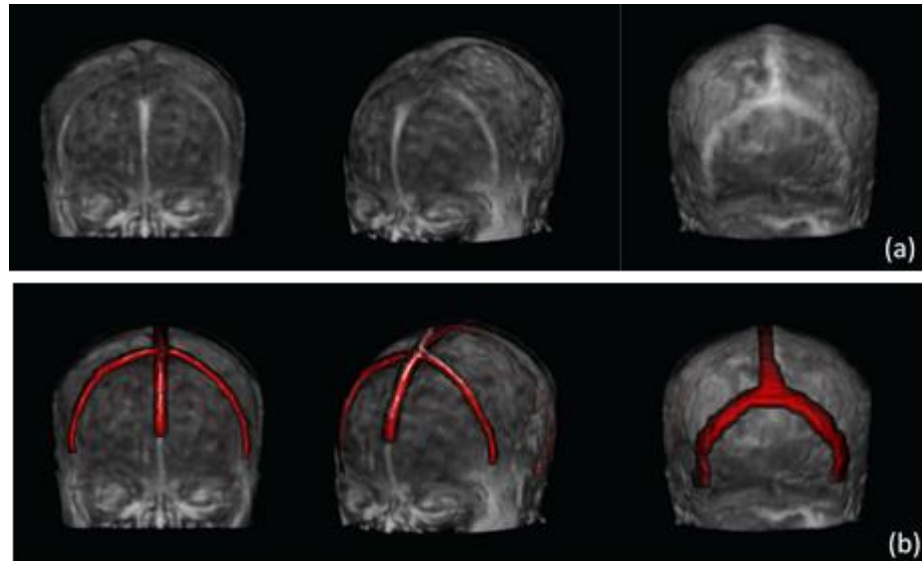
**Fig. 10.** Manual extraction of sutures from MR image of subject N3. a) The sutures are visible as bright tracks in the 3D view of the head, b) Overlay of extracted voxels as anatomical landmarks in red with MR image.

## Algorithm. 1

*A = Ground truth*

*B = The segmented image containing the skull*

*SI = Similarity Index*

*L=Number of nonzero elements of A*

*MSI: If A (i, j, k) == 1 && B (i, j, k) == 1 → counter=1*

$$MSI = \frac{\sum_A counter}{L}$$

*MSI_1: If A (i, j, k) == 1 && if B($\alpha$, $\beta$, $\gamma$) $\in$ { (i, j, k) | B (i-1: i+1, j-1: j+1, k-1: k+1) == 1} → counter=1*

$$MSI\_1 = \frac{\sum_A counter}{L}$$

*MSI_2: If A (i, j, k) == 1 && if B($\alpha$, $\beta$, $\gamma$) $\in$ { (i, j, k) | B (i-2: i+2, j-2: j+2, k-2: k+2) == 1} → counter=1*

$$MSI\_2 = \frac{\sum_A counter}{L}$$

### 2.4.2 Evaluation of the results using the size of fontanels

At birth, the normal size of the anterior fontanel in infants is in the range of 0.6 to 3.6 cm (Kiesler & Ricer, 2003. Therefore, it can also be considered as a criterion to assess skulls extracted from MR images. To calculate the size of the anterior fontanel, the proposed method in (Kiesler & Ricer, 2003)  has been used. The anterior fontanel is similar to a rhombus and its size will be equal to the average of small and large diameters as shown in Figure 12.
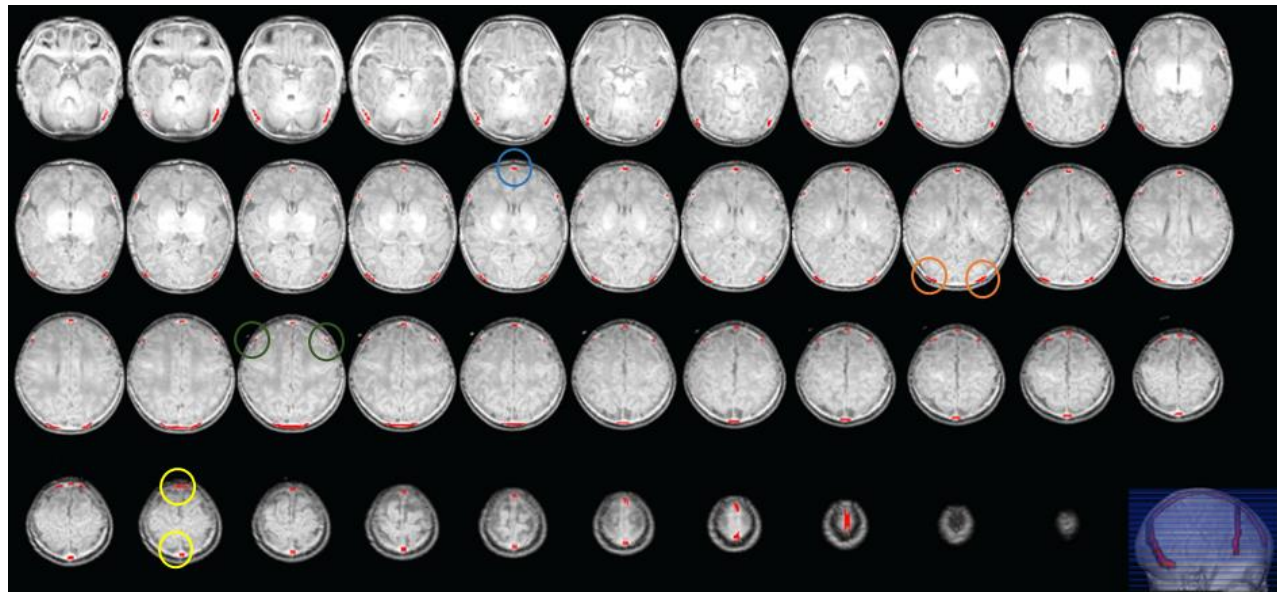
**Fig. 11.** Axial MR slices of the subject N3. Red tracks in each slice show the anatomical landmarks corresponding to sutures which were manually extracted. The blue, green, orange and yellow circles enclose a metopic, coronal, lambdoid and sagittal suture, respectively.
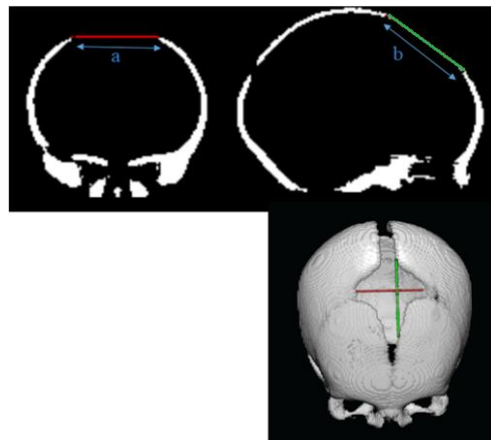


**Fig. 12.** Anterior fontanel size is computed by averaging the length of its small (a) and large (b) diameters.

### 2.4.3 Evaluation of the results using the skull thickness

Another criterion that can be used to validate the proposed method is the skull thickness. (Li et al., 2015) showed that the thickness of the skull increases gradually and inhomogeneously from birth. To calculate the thickness of the extracted skulls, after removing the extracted facial bones by 3DSlicer software, the inner and outer surfaces of the skull were extracted using the coupled level sets algorithm presented by (Ghadimi et al., 2015). Then the average distance between the two acquired surfaces was reported as bone thickness.

### 2.4.4 Evaluation of the results using an MR-CT image

The skull segmentation method can also be evaluated using MR and CT images which have been acquired from a neonate within a short time interval. To perform this evaluation, the CT image must be in the same space as the MR image. For this purpose, the multimodal registration method described in Section 2.3.2 is used. Then, the cranial bones are extracted from the CT image via thresholding and considered as a ground truth. For comparison, the dice similarity coefficient (DSC) and modified Hausdorff distance (MHD) are used (Dice, 1945; Dubuisson & Jain, 1994). In this experiment, the CT and MR images were acquired from a subject at 40- and 42-weeks GA, respectively. Figure 13 shows the CT and MR images of the test subject after registration.
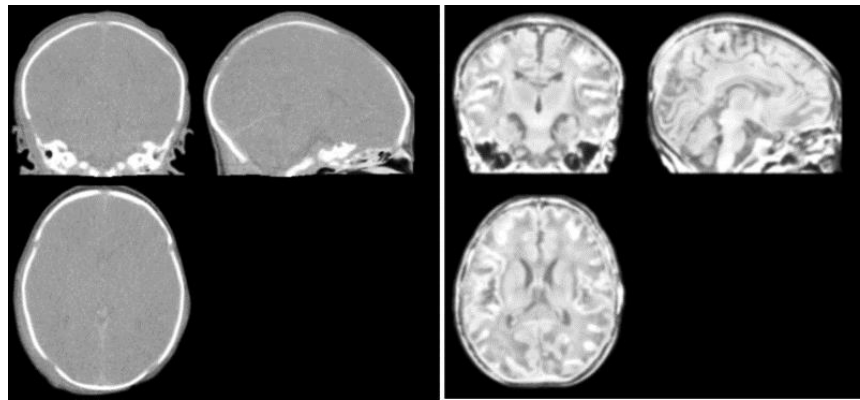


**Fig. 13.** The corresponding CT and MR images of the subject Test1 after multimodal registration

## 3. Results

### 3.1 Evaluation of the results using 3D anatomical landmarks

Figure 14, illustrates the match between the position of extracted anatomical landmarks (anterior and posterior sutures) and cranial bones which have been segmented by the proposed algorithm. The second, fourth and sixth column in Table 1 indicate the evaluation of the segmented MR images using MSI, MSI_1 and MSI_2 indices. Obviously, the values closer to one, represent more accurate results. It is noteworthy that the above indices represent the similarity in shape between reconstructed sutures and corresponding landmarks. The low values of MSI in Table 1 are mainly due to the fact that the coronal and lambdoid sutures were extracted as closed by the proposed algorithm. The results of Ghadimi's algorithm (Ghadimi, 2017) are indicated in the third, fifth and seventh column of Table 1. They are generally lower than ours which demonstrate the superiority of the proposed method. As well, the surface of the skull in Ghadimi's method (Ghadimi, 2017) had many protrusions and depressions, and in some cases, it had discontinuities, which have been improved in this research.
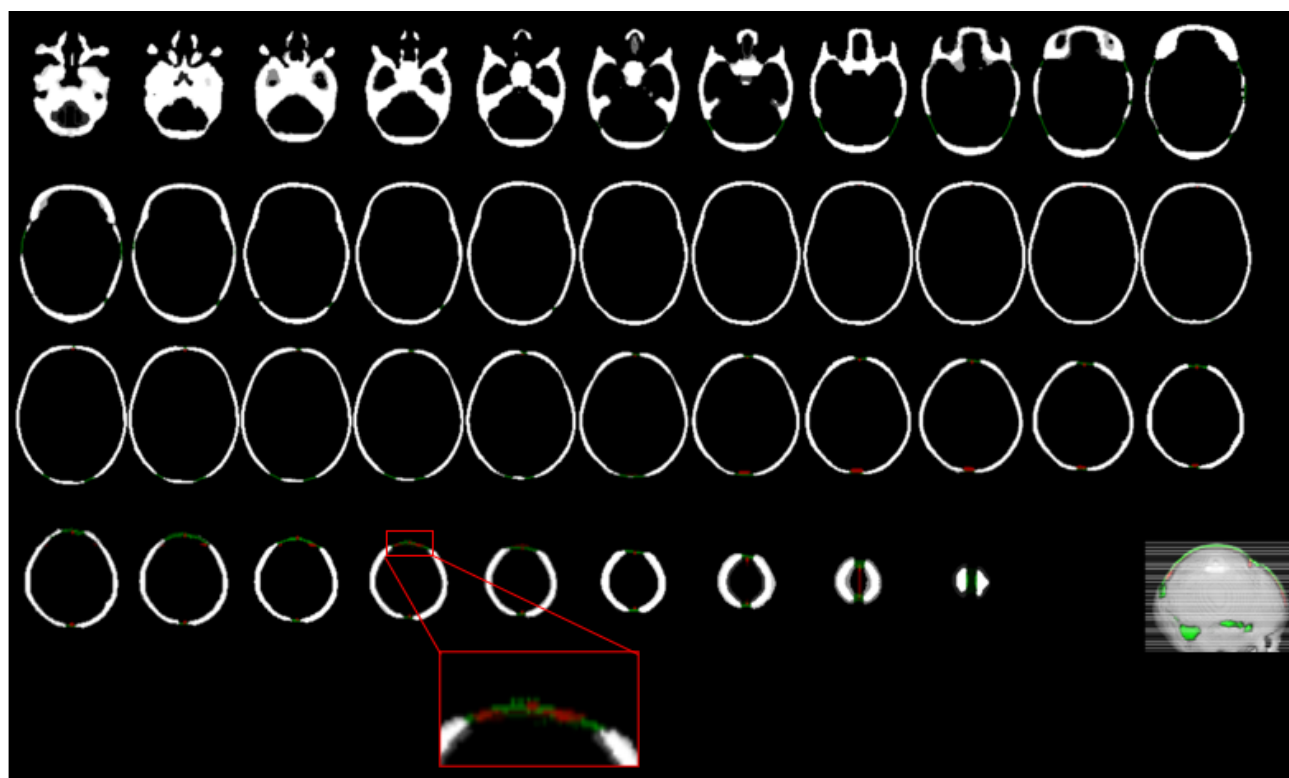
**Fig. 14.** Axial view of the N1 subject image. Red tracks in each slice show the anatomical landmarks corresponding to sutures. Green tracks in each slice show the fontanels reconstructed using the coupled level set algorithm (Ghadimi et al., 2015).

**Table 1.**

Evaluation of the proposed skull segmentation method using MSI, MSI_1 and MSI_2 similarity coefficients. The two last columns show the size of the anterior fontanel and average skull thickness computed from the segmented cranial bones.

| Subjects | MSI | MSI* | MSI_1 | MSI_1* | MSI_2 | MSI_2* | Anterior fontanel size (cm) | Average skull thickness (mm) |
|---|---|---|---|---|---|---|---|---|
| N1 | 0.23 | 0.05 | 0.85 | 0.28 | 0.97 | 0.33 | 3.5 | 1.80 |
| N2 | 0.13 | 0.06 | 0.56 | 0.30 | 0.78 | 0.41 | 3.34 | 1.78 |
| N3 | 0.10 | 0.06 | 0.61 | 0.23 | 0.87 | 0.31 | 3.47 | 1.66 |
| N4 | 0.03 | 0 | 0.38 | 0.12 | 0.92 | 0.41 | 3.39 | 1.67 |
| N5 | 0.13 | NaN** | 0.41 | **NaN**** | 0.70 | **NaN**** | 3.73 | 2.40 |
| N6 | 0.02 | 0 | 0.63 | 0.18 | 0.97 | 0.53 | 3.57 | 2.37 |
| N7 | 0.34 | 0.08 | 0.92 | 0.25 | 0.97 | 0.30 | 3.23 | 1.76 |
| T1 | 0.18 | 0.11 | 0.85 | 0.37 | 0.93 | 0.48 | 2.70 | 1.90 |
| T2 | 0.30 | 0.08 | 0.89 | 0.32 | 0.99 | 0.41 | 3.13 | 1.85 |
| T3 | 0.24 | **0.12** | 0.87 | 0.41 | 0.92 | 0.48 | 2.64 | 1.83 |
| T4 | 0.10 | **0.03** | 0.27 | 0.13 | 0.42 | 0.18 | 2.89 | 1.84 |
| T5 | 0.03 | **NaN**** | 0.20 | **NaN**** | 0.71 | **NaN**** | 2.96 | 1.75 |
| T6 | 0.11 | **NaN**** | 0.50 | **NaN**** | 0.88 | **NaN**** | 3.05 | 2.01 |
| T7 | 0.31 | **NaN**** | 0.91 | **NaN**** | 0.97 | **NaN**** | 3.08 | 1.70 |
| Average | 0.16 ± **0.11** | 0.06 ± **0.04** | 0.63 ± **0.25** | 0.26 ± 0.1 | 0.86 ± 0.16 | 0.38 ± .11 | 3.19±0.33 | 1.88±0.23 |

\* Result obtained by the method in (Ghadimi, 2017)

\*\* No information available

### 3.2 Evaluation of the results using the size of fontanels

The eighth column of Table 1 shows the size of the anterior fontanel of all segmented images. As shown, its average value is 3.19 cm, which corresponds to the normal range (Mohtasebi et al., 2021).

### 3.3 Evaluation of the results using the skull thickness

The average value of the extracted bone thickness for 14 newborn MR images is 1.88 mm, which is close to 2.16 mm reported by (Li et al., 2015) for healthy infants. The results in the last column of Table 1 confirm the success of the proposed method.

### 3.4 Evaluation using an MR-CT image

Figure 15 shows the superposition of the skull extracted from the MR image (white) and that extracted from the CT image (red). For the segmentation of this MR image, probabilities less than 0.5 were considered as zero in the created probability models. DSC, between skulls extracted from MR and CT images, is 0.50 and MHD is 1.60 mm. The CT scan of this subject was taken two weeks before the MR one. Therefore, according to the growth charts of neonatal head circumference from birth to 13 weeks, prepared by the World Health Organization (Mercedes de Onis et al, 2007), we expect that the head circumference is larger in MR image due to growth of the infant (Figure 15). Accordingly, the low value of DSC is partially justified by the difference in the size of the skull in CT and MR images. The head circumference is 355 mm and 368mm in the CT and MR image, respectively. According to the WHO Child Growth Standards (Mercedes de Onis et al, 2007) we expect the head circumference difference to be around 1.5 cm on average during this period, so the difference of 1.3 cm seems acceptable.
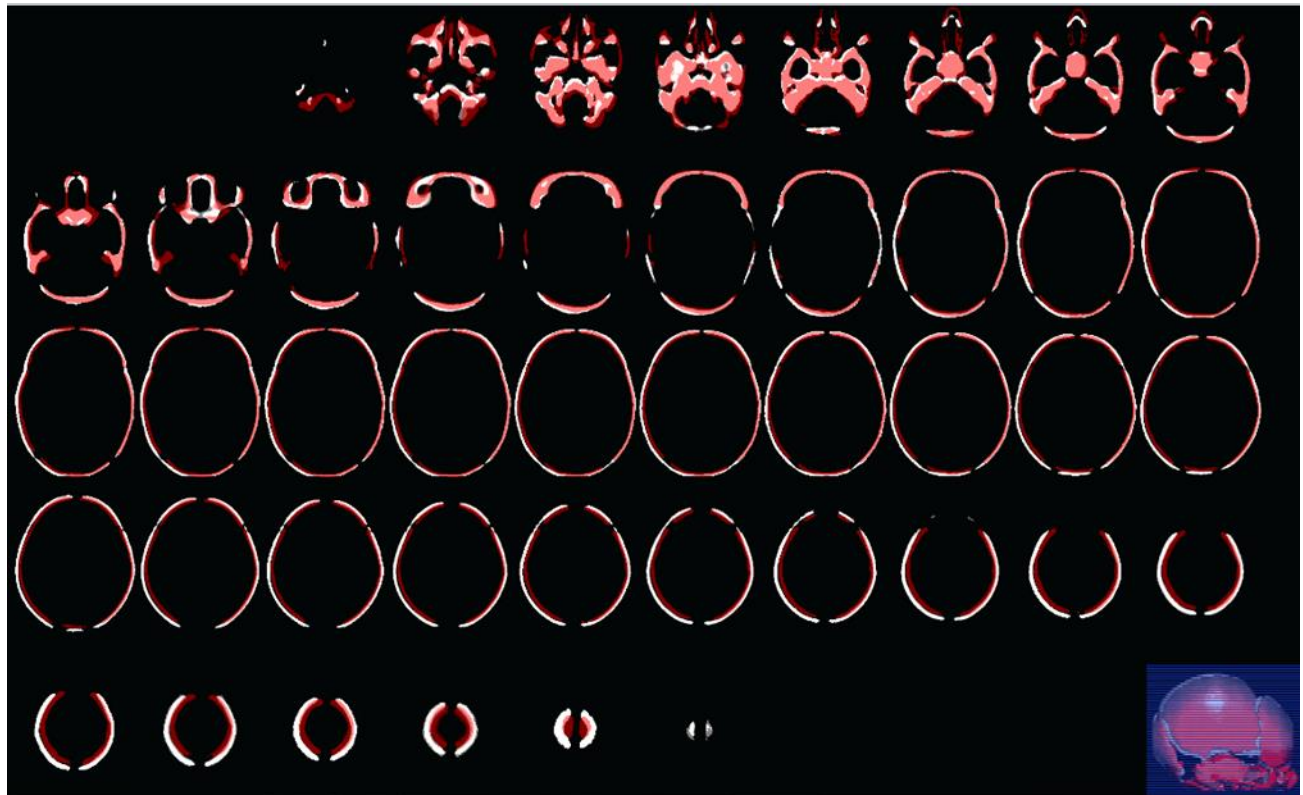
**Fig. 15**. Evaluation of the skull segmentation method using CT and MR data acquired from a neonate in 40- and 42-weeks GA, respectively. The extracted skull from MR image (white) is superposed on the extracted skull from corresponding CT image (red).

## 4. Discussion

The effect of fontanels and sutures on EEG and MEG source analysis using realistic neonatal head models was investigated by several studies (Azizollahi et al., 2016; Dehaes et al., 2013; Lew et al., 2013; Noreika et al., 2020; Odabaee et al., 2014; Roche-Labarbe et al., 2008). Realistic models of a neonates' head as created by MR imaging are commonly used to identify different tissues in the head that exhibit different electrical and optical properties. Accordingly, accurate skull segmentation of neonatal brain MRIs can have a significant impact on the results of neonatal functional analysis using EEG, MEG, near infrared spectroscopy (NIRS) and functional MRI (fMRI). Unfortunately, the MRI data does not provide perceivable information needed to localize the cranial bones in the neonatal head image. Accordingly, a bimodal approach based on MRI and CT images of infants' head was proposed for the first time in this paper to solve the challenging problem of skull segmentation from MRIs. The proposed approach relies on retrospective MR and CT images in order to create subject-specific atlases of the neonatal head including probability maps of the skull, scalp and CSF. These subject-specific atlases are employed by an EM algorithm in conjunction with Markov random filed model to segment skull from neonatal head MRI data acquired from a subject. Our approach consisted of three main blocks. In the first block, subject-specific head and intracranial templates and CSF probability map are created using retrospective MR data acquired from neonates of 39-42 weeks GA. In the second block, the head and intracranial MR templates are employed to create a subject-specific CT head template using retrospective CT data acquired from neonates in the same age range. The third block uses the CT head template in order to create subject-specific probability maps of skull and scalp. Finally, the subject-specific CSF, skull and scalp probability maps are fed to an EM algorithm in conjunction with Markov random field model, as implemented in FSL software, in order to segment skull from the input MR image. The proposed approach provided realistic segmentation of skull in which fontanel and sutures were taken into consideration.

The evaluation of the proposed neonatal skull segmentation approach was another challenge to overcome due to the lack of ground truth. Former methods for neonatal skull segmentation from MRI have often used manual or semi-automatic segmentation of image slices as ground truth (Mahapatra, 2012, Shi et al., 2012, Yamaguchi et al., 2010). In some studies, only a few slices have been segmented and used as ground truth due to invisibility of cranial bones in certain slices and time-consuming process of manual segmentation. On the other hand, most of these methods, ignored sutures and fontanels (Despotovic et al., 2009, Burguet et al., 2004). In other words, they considered the skull as a continuous and homogenous tissue which was far from a realistic skull geometry in neonates (Despotovic et al., 2009, Burguet et al., 2004). The issues raised underscore the need for a trusted ground truth to assess the results. We noticed that in spite of quasi-invisibility of cranial bones, the sutures are perceivable as bright regions in the three-dimensional volume rendering of the neonatal head in T1-weighted MR image. Therefore, they were considered as three-dimensional landmarks and used as ground truth. Accordingly, we reconstructed the sutures from skull segmentation results and then compared them with the sutures which have been extracted manually from the original MR data as ground truth. For this purpose, modified versions of Dice similarity index were introduced throughout this paper.

An alternative reliable solution to evaluate our neonatal skull segmentation method is appealing to retrospective bimodal MR-CT head data from the same neonates which have been acquired within a short time interval. Obviously, the access to such bimodal data is very restricted due to several factors. First, acquiring CT images from neonates is rarely authorized when there are strong clinical reasons. Second, finding bimodal MR-CT data which have been acquired from neonates with normal head anatomy is challenging because in most cases the subjects were suffering from some kind of abnormality in their head such as bleeding, concussion, etc. Third, the time interval between MR and CT acquisition must be sufficiently short due to rapid development of the skull in neonates. In this paper, the bimodal data acquired from only one subject was employed for evaluating the proposed neonatal skull segmentation method. Taking advantage of more bimodal test data would be helpful for an exhaustive evaluation of the proposed method.

The proposed method outperformed its close counterparts in terms of modified similarity indices notably MSI_2. The creation and use of subject-specific atlases justifies the superiority of the proposed approach over Ghadimi's method (Ghadimi, 2017) which suggests creating atlases in the newborn stereotaxic space (Kazemi et al., 2007). On the other hand, in the method proposed by Kazemi et al. (Kazemi et al., 2008), the skull probability map was created as a continuous structure without considering sutures and fontanels. Obviously, including sutures and fontanels is mandatory to achieve a realistic segmentation of the skull from MR images.

In this study, a limited number retrospective MR and CT images were used to create the subject specific atlases. Obviously, using larger datasets of each modality which include skulls with diverse morphologies may improve the generalization property of the created atlases. Furthermore, one may use a multi-atlas approach to be able to create a specific atlas which is closer to the subject's head geometry. However, the access to such a large dataset with normal head geometry particularly in CT modality is a challenging issue. The multimodal atlas data should also include manually extracted tissues such as intracranial, CSF, skull and scalp for being used in the creation of subject-specific atlas and probability maps.

## 5. Conclusion

An atlas-based bimodal MR-CT approach for realistic skull segmentation in neonatal MR data was proposed in this study. The new approach deploys preprocessed retrospective MR and CT head data in order to create subject-specific MR and CT head templates. It creates also the subject-specific CSF, skull and scalp probability maps using the semiautomatically extracted CSF (from atlas MRIs), skull and scalp (from atlas CT scans) tissues. The resulted subject-specific MR atlas and CSF, skull and scalp probability maps are used within the framework of EM algorithm in conjunction with Markov random filed model to segment the skull from an input neonatal head MRI. The proposed approach provided realistic skull segmentation results which included sutures and fontanels. The evaluation of the results using four elaborated evaluation procedures demonstrated the good performance of the proposed algorithm. The proposed skull segmentation method seems promising in neurodevelopmental and neuroscience studies.

## Acknowledgements

# References

Avants, B. B., Epstein, C. L., Grossman, M., & Gee, J. C. (2008). Symmetric diffeomorphic image registration with cross-correlation: evaluating automated labeling of elderly and neurodegenerative brain. *Med Image Anal*, *12*(1), 26-41. https://doi.org/10.1016/j.media.2007.06.004

Avants, B. B., Tustison, N. J., Stauffer, M., Song, G., Wu, B., & Gee, J. C. (2014). The Insight ToolKit image registration framework. *Front Neuroinform*, *8*, 44. https://doi.org/10.3389/fninf.2014.00044

Azizollahi, H., Aarabi, A., & Wallois, F. (2016). Effects of uncertainty in head tissue conductivity and complexity on EEG forward modeling in neonates. *Hum Brain Mapp*, *37*(10), 3604-3622. https://doi.org/10.1002/hbm.23263

Burguet, J., Gadi, N., & Bloch, I. (2004). Realistic models of children heads from 3D-MRI segmentation and tetrahedral mesh construction. Proceedings. 2nd International Symposium on 3D Data Processing, Visualization and Transmission, 2004. 3DPVT 2004., https://doi.org/10.1109/TDPVT.2004.1335298

Cherel, M., Budin, F., Prastawa, M., Gerig, G., Lee, K., Buss, C., Lyall, A., Consing, K. Z., & Styner, M. (2015). Automatic tissue segmentation of neonate brain MR Images with subject-specific atlases. Medical Imaging 2015: Image Processing, https://doi.org/10.1117/12.2082209

Daliri, M., Moghaddam, H. A., Ghadimi, S., Momeni, M., Harirchi, F., & Giti, M. (2010). Skull segmentation in 3D neonatal MRI using hybrid Hopfield Neural Network. 2010 Annual International Conference of the IEEE Engineering in Medicine and Biology, https://doi.org/10.1109/iembs.2010.5627619

Dehaes, M., Kazemi, K., Pelegrini-Issac, M., Grebe, R., Benali, H., & Wallois, F. (2013). Quantitative effect of the neonatal fontanel on synthetic near infrared spectroscopy measurements. *Hum Brain Mapp*, *34*(4), 878-889. https://doi.org/10.1002/hbm.21483

Despotovic, I., Deburchgraeve, W., Hallez, H., Vansteenkiste, E., & Philips, W. (2009). Development of a realistic head model for EEG event-detection and source localization in newborn infants. 2009 Annual International Conference of the IEEE Engineering in Medicine and Biology Society, https://doi.org/10.1109/IEMBS.2009.5335052

Dice, L. R. (1945). Measures of the amount of ecologic association between species. *Ecology*, *26*(3), 297-302. https://doi.org/https://doi.org/10.2307/1932409

Dubuisson, M.-P., & Jain, A. K. (1994). A modified Hausdorff distance for object matching. Proceedings of 12th international conference on pattern recognition, https://doi.org/10.1109/ICPR.1994.576361

Fedorov, A., Beichel, R., Kalpathy-Cramer, J., Finet, J., Fillion-Robin, J.-C., Pujol, S., Bauer, C., Jennings, D., Fennessy, F., & Sonka, M. (2012). 3D Slicer as an image computing platform for the Quantitative Imaging Network. *Magnetic resonance imaging*, *30*(9), 1323-1341. https://doi.org/10.1016/j.mri.2012.05.001

Ghadimi, S. (2017). Creation of 3D neonatal skull model using MR and CT images. *K. N. Toosi University of technology and university of Picardie Jules Verne*, *Doctoral dissertation*.

Ghadimi, S., Moghaddam, H. A., Grebe, R., & Wallois, F. (2015). Skull segmentation and reconstruction from newborn CT images using coupled level sets. *IEEE journal of biomedical and health informatics*, *20*(2), 563-573. https://doi.org/10.1109/JBHI.2015.2391991

Ghadimi, S., Mohtasebi, M., Abrishami Moghaddam, H., Grebe, R., Gity, M., & Wallois, F. (2017). A Neonatal Bimodal MR-CT Head Template. *PloS one*, *12*(1), e0166112. https://doi.org/10.1371/journal.pone.0166112

Henkelman, R. M., Watts, J. F., & Kucharczyk, W. (1991). High signal intensity in MR images of calcified brain tissue. *Radiology*, *179*(1), 199-206. https://doi.org/10.1148/radiology.179.1.1848714

Kazemi, K., Ghadimi, S., Abrishami-Moghaddam, H., Grebe, R., Gondry-Jouet, C., & Wallois, F. (2008). Neonatal probabilistic models for brain, CSF and skull using T1-MRI data: preliminary results. 2008 30th Annual International Conference of the IEEE Engineering in Medicine and Biology Society, https://doi.org/10.1109/IEMBS.2008.4650060

Kazemi, K., Moghaddam, H. A., Grebe, R., Gondry-Jouet, C., & Wallois, F. (2007). A neonatal atlas template for spatial normalization of whole-brain magnetic resonance images of newborns: preliminary results. *Neuroimage*, *37*(2), 463-473. https://doi.org/10.1016/j.neuroimage.2007.05.004

Keith A. Johnson, M.D. *Brigham and Women`s Hospital, Harvard Medical School* https://www.med.harvard.edu/aanlib/hem.html. (accessed 23 April 2022)

Kiesler, J., & Ricer, R. (2003). The abnormal fontanel. *Am Fam Physician*, *67*(12), 2547-2552. https://www.ncbi.nlm.nih.gov/pubmed/12825844

Lemieux, L., Wieshmann, U. C., Moran, N. F., Fish, D. R., & Shorvon, S. D. (1998). The detection and significance of subtle changes in mixed-signal brain lesions by serial MRI scan matching and spatial normalization. *Med Image Anal*, *2*(3), 227-242. https://doi.org/10.1016/s1361-8415(98)80021-2

Lew, S., Sliva, D. D., Choe, M. S., Grant, P. E., Okada, Y., Wolters, C. H., & Hamalainen, M. S. (2013). Effects of sutures and fontanels on MEG and EEG source analysis in a realistic infant head model. *Neuroimage*, *76*, 282-293. https://doi.org/10.1016/j.neuroimage.2013.03.017

Li, Z., Park, B. K., Liu, W., Zhang, J., Reed, M. P., Rupp, J. D., Hoff, C. N., & Hu, J. (2015). A statistical skull geometry model for children 0-3 years old. *PloS one*, *10*(5), e0127322. https://doi.org/10.1371/journal.pone.0127322

Mahapatra, D. (2012). Skull stripping of neonatal brain MRI: using prior shape information with graph cuts. *Journal of digital imaging*, *25*(6), 802-814. https://doi.org/10.1007/s10278-012-9460-z

Mohtasebi, M., Bayat, M., Ghadimi, S., Moghaddam, H. A., & Wallois, F. (2021). Modeling of Neonatal Skull Development Using Computed Tomography Images. *Irbm*, *42*(1), 19-27. https://doi.org/10.1016/j.irbm.2020.02.002

Nielsen, J. D., Madsen, K. H., Puonti, O., Siebner, H. R., Bauer, C., Madsen, C. G., Saturnino, G. B., & Thielscher, A. (2018). Automatic skull segmentation from MR images for realistic volume conductor models of the head: Assessment of the state-of-the-art. *Neuroimage*, *174*, 587-598. https://doi.org/10.1016/j.neuroimage.2018.03.001

Noorizadeh, N., Kazemi, K., Danyali, H., & Aarabi, A. (2019). Multi-atlas based neonatal brain extraction using a two-level patch-based label fusion strategy. *Biomedical Signal Processing and Control*, *54*, 101602. https://doi.org/10.1016/j.bspc.2019.101602

Noreika, V., Georgieva, S., Wass, S., & Leong, V. (2020). 14 challenges and their solutions for conducting social neuroscience and longitudinal EEG research with infants. *Infant Behavior and Development*, *58*, 101393. https://doi.org/10.1016/j.infbeh.2019.101393

Odabaee, M., Tokariev, A., Layeghy, S., Mesbah, M., Colditz, P. B., Ramon, C., & Vanhatalo, S. (2014). Neonatal EEG at scalp is focal and implies high skull conductivity in realistic neonatal head models. *Neuroimage*, *96*, 73-80. https://doi.org/10.1016/j.neuroimage.2014.04.007

Okada, E., & Delpy, D. T. (2003). Near-infrared light propagation in an adult head model. I. Modeling of low-level scattering in the cerebrospinal fluid layer. *Appl Opt*, *42*(16), 2906-2914. https://doi.org/10.1364/ao.42.002906

Otsu, N. (1979). A threshold selection method from gray-level histograms. *IEEE transactions on systems, man, and cybernetics*, *9*(1), 62-66. https://doi.org/10.1109/TSMC.1979.4310076

Prastawa, M., Gilmore, J. H., Lin, W., & Gerig, G. (2005). Automatic segmentation of MR images of the developing newborn brain. *Med Image Anal*, *9*(5), 457-466. https://doi.org/10.1016/j.media.2005.05.007

Roche-Labarbe, N., Aarabi, A., Kongolo, G., Gondry-Jouet, C., Dumpelmann, M., Grebe, R., & Wallois, F. (2008). High-resolution electroencephalography and source localization in neonates. *Hum Brain Mapp*, *29*(2), 167-176. https://doi.org/10.1002/hbm.20376

Rorden, C., Bonilha, L., Fridriksson, J., Bender, B., & Karnath, H. O. (2012). Age-specific CT and MRI templates for spatial normalization. *Neuroimage*, *61*(4), 957-965. https://doi.org/10.1016/j.neuroimage.2012.03.020

Shi, F., Wang, L., Dai, Y., Gilmore, J. H., Lin, W., & Shen, D. (2012). LABEL: pediatric brain extraction using learning-based meta-algorithm. *Neuroimage*, *62*(3), 1975-1986. https://doi.org/10.1016/j.neuroimage.2012.05.042

Smith, S. M., Jenkinson, M., Woolrich, M. W., Beckmann, C. F., Behrens, T. E., Johansen-Berg, H., Bannister, P. R., De Luca, M., Drobnjak, I., & Flitney, D. E. (2004). Advances in functional and structural MR image analysis and implementation as FSL. *Neuroimage*, *23*, S208-S219. https://doi.org/10.1016/j.neuroimage.2004.07.051

Tustison, N. J., Avants, B. B., Cook, P. A., Zheng, Y., Egan, A., Yushkevich, P. A., & Gee, J. C. (2010). N4ITK: improved N3 bias correction. *IEEE Trans Med Imaging*, *29*(6), 1310-1320. https://doi.org/10.1109/TMI.2010.2046908

Weinreb, J. C., Brateman, L., Babcock, E. E., Maravilla, K. R., Cohen, J. M., & Horner, S. (1985). Chemical shift artifact in clinical magnetic resonance images at 0.35 T. *American journal of roentgenology*, *145*(1), 183-185. https://doi.org/10.2214/ajr.145.1.183

Mercedes de Onis et al. (2007). WHO child growth standards: head circumference-for-age, arm circumference-for-age, triceps skinfold-for-age and subscapular skinfold-for-age: methods and development. ISBN 978 92 4 154718 5. Downloadable from https://www.who.int/publications/i/item/9789241547185. (accessed 23 April 2022)

Yamaguchi, K., Fujimoto, Y., Kobashi, S., Wakata, Y., Ishikura, R., Kuramoto, K., Imawaki, S., Hirota, S., & Hata, Y. (2010). Automated fuzzy logic-based skull stripping in neonatal and infantile MR images. International Conference on Fuzzy Systems, https://doi.org/10.1109/FUZZY.2010.5584839